

Numerical simulation of baroclinic waves with a parameterized boundary layer

R. S. Plant* and S. E. Belcher

Joint Centre for Mesoscale Meteorology, University of Reading

PO Box 243, Reading, Berkshire, RG6 6BB, UK.

March 16, 2007

*r.s.plant@rdg.ac.uk Corresponding author.

Abstract

A dry three-dimensional baroclinic life cycle model is used to investigate the role of turbulent fluxes of heat and momentum within the boundary layer on mid-latitude cyclones. Simulations are performed of life cycles for two basic states, both with and without turbulent fluxes. The different basic states produce cyclones with contrasting frontal and mesoscale-flow structures. The analysis focuses on the generation of potential-vorticity (PV) in the boundary layer and its subsequent transport into the free troposphere. The dynamic mechanism through which friction mitigates a barotropic vortex is that of Ekman pumping. This has often been assumed to be also the dominant mechanism for baroclinic developments. The PV framework highlights an additional, baroclinic mechanism. Positive PV is generated baroclinically due to friction to the north-east of a surface low and is transported out of the boundary layer by a cyclonic conveyor belt flow. The result is an anomaly of increased static stability in the lower troposphere which restricts the growth of the baroclinic wave. The reduced coupling between lower and upper levels can be sufficient to change the character of the upper-level evolution of the mature wave. The basic features of the baroclinic damping mechanism are robust for different frontal structures, with and without turbulent heat fluxes, and for the range of surface roughness found over the oceans.

1. Introduction

It is well established that the development of some mid-latitude cyclones is highly sensitive to the turbulent fluxes of momentum, heat and moisture in the boundary layer. For example, Anthes and Keyser (1979) described a 24h mesoscale-model simulation which produced a cyclone more than 20hPa shallower with the inclusion of friction. Indeed, the extent to which friction is capable of damping (or even of suppressing) baroclinic developments is a long-standing and much-debated issue (Farrell 1986, 1989; Valdes and Hoskins 1988; Moore and Montgomery 2004). Within such discussions, the dominant effect of friction is often assumed to be Ekman pumping. As described by Holton (1992) for instance, boundary layer convergence just above a surface low center induces low-level ascent which will act to spin-down a barotropic circulation.

The potential vorticity (PV) framework is a powerful one for elucidating the dynamics of baroclinic systems (Hoskins et al. 1985). In this language, Ekman pumping dampens a low-level cyclonic circulation through a reduction of PV above the low center (Sec. 3). However, there is good evidence that other boundary layer processes are active in generating and redistributing low-level PV. Nakamura and Held (1989), for instance, showed that frontal occlusion can extract PV from the reservoir associated with a surface temperature gradient. Later Cooper et al. (1992) argued persuasively against any special role for occlusion. They identified several mechanisms (discussed in Sec. 3) through which turbulent fluxes of heat and momentum may generate positive PV. Indeed, a significant increase in domain-averaged PV was found to occur when a simple boundary-layer turbulence parameterization was added to the two-dimensional Eady model. This study was extended by Stoelinga's (1996) partitioning of the generated PV in a marine cyclone simulated by a full mesoscale model. For the particular case examined, the boundary-layer parameterization acted to reduce the overall low-level PV, but friction was found to be responsible for a positive

anomaly in the vicinity of the bent-back warm front (see their Fig. 7(e)). Frictional generation of positive PV was also identified in a continental cyclone by Davis et al. (1993). These results show that attempts to understand the interactions between boundary-layer and synoptic-scale dynamics in terms of Ekman pumping are incomplete.

Recently Adamson et al. (2006) (hereafter ABHP) studied the frictional generation of PV in a baroclinic wave, and the subsequent transport of that PV into the interior of the flow. Their emphasis on transport out of the boundary layer is important, since “PV-thinking” is based on the presence of a balanced flow. The simulations were intermediate in complexity between those of Cooper et al. (1992) and Stoelinga (1996). A parameterization of turbulent momentum fluxes was included within a three-dimensional, dry, primitive-equation model of a baroclinic life cycle. Such a setup permitted relatively straightforward identification and interpretation of the PV changes produced by friction.

The results confirmed that Ekman pumping produces a negative PV anomaly, but this remains confined to the lower part of the boundary layer. However, a positive PV anomaly was also generated through the action of friction. This occurred through a baroclinic mechanism. Figure 1 illustrates those regions within a mid-latitude cyclone that are favorable for PV generation through the baroclinic mechanism. (The figure is taken from ABHP and is based on the structure of a linear baroclinic wave.) The main source area is to the east and north-east of the surface low center. In the life cycle studied by ABHP, PV generated in that area was transported by the ascending warm conveyor belt into the free troposphere and then westwards (in a system relative sense) towards the low center. A positive PV anomaly formed over the low center, just above the boundary layer. The anomaly was constrained to a thin layer in the vertical, at least in part due to the Ekman circulation (Xu et al. 1988). Such a thin anomaly of PV is associated with high static stability (Hoskins

et al. 1985). Thus, although the inversion of such an anomaly may yield a cyclonic circulation (see Stoelinga (1996)), it nonetheless acts to dampen the development of a baroclinic wave by reducing the coupling between the surface and upper-level waves.

[Figure 1 about here.]

ABHP's picture is an appealing synthesis of their own and previous results. However, it is unclear whether it provides a generic description of frictional effects in mid-latitude cyclones. For instance, although Fig. 1 was deduced for a baroclinic wave in its linear phase, ABHP argued that it should identify the source area of PV generation in general. This claim requires testing. Moreover, even if the location of the source area is robust, transport of the generated PV might prove to be different for a cyclone with different mesoscale flow structures.

Other issues concern the effects of turbulent heat and moisture fluxes, which were not included in the simulations of ABHP. Such effects may be important when extending the ideas of ABHP from idealized baroclinic waves to fully-realistic mid-latitude cyclones. Although turbulent fluxes of moisture can reasonably be ignored in many cases, they sometimes are crucial for cyclones in which latent heating plays an important role (Uccellini et al. 1987). Similarly, turbulent fluxes of sensible heat only have a modest impact on cyclone development in general (e.g., Ahmadi-Givi et al. 2004; Reed et al. 1992, Table 2). However, sensible heat fluxes do provide an important control on boundary-layer depth and stability and one might question whether a thin, high-static-stability anomaly just above the boundary layer can survive their inclusion.

In this paper we develop the study of ABHP by considering another type of frontal development and other boundary layer processes. Our motivations are twofold. First, as we have discussed above, there are some important issues concerning the robustness of the ABHP picture. Second, the simulations described here should provide a valuable intermediate step between an idealized

model and a full mesoscale model. It is non-trivial in a mesoscale model to isolate the interactions of friction, turbulent heat fluxes and large-scale dynamics in a satisfactory way. The task is rather more feasible, however, in the present context where a simple boundary-layer parameterization is used in the simulation of baroclinic waves. It is expected that the understanding gained from these simulations will provide a useful guide and comparison for the more complex issues of boundary layer dynamics in forecast models.

The rest of this paper is structured as follows: Sec. 2 describes the simulations performed and Sec. 3 discusses the physical processes that can generate PV within the boundary layer. The effects of the boundary layer parameterization on large-scale dynamics generally and low-level frontal structures in particular are described in Secs. 4 and 5 respectively. The scene is then set for a discussion of the low-level PV evolution, both without (Sec. 6) and with (Sec. 7) turbulent fluxes of sensible heat included in the simulations. In Sec. 8 we consider how anomalous low-level PV restricts the growth rate of the baroclinic wave. Following some remarks on the effects of varying the surface roughness (Sec. 9), conclusions are presented in Sec. 10, while an Appendix provides details of the boundary-layer parameterization.

2. IGCM Simulations

As in ABHP, the simulations are performed with the Reading Intermediate General Circulation Model (IGCM) (Hoskins and Simmons 1975), which solves the dry, primitive equations with a spectral representation of variables in the horizontal and a sigma co-ordinate in the vertical. The model has been successfully used for a number of studies of baroclinic life cycles (for example Simmons and Hoskins 1980; Thorncroft et al. 1993, and references therein). The resolution used here is T42 L19, and life cycles are initialized by adding to the basic state the fastest growing

normal mode (normalized to have a surface pressure perturbation of 1hPa) with wavenumber six. Horizontal hyperdiffusion is applied by the ∇^6 operator with a decay rate for the shortest retained wavelength of $4h^{-1}$.

Surface temperature is prescribed as a function of latitude only and held fixed in the simulations. The boundary layer parameterization¹ uses a combination of the Charnock relation and Monin-Obukhov similarity theory in the surface layer, and above that a simple scheme based on the mixing length approach of Louis (1979). Details can be found in ABHP. Here the scheme has been extended to include turbulent fluxes of sensible heat. For completeness, the additional expressions required are stated in Appendix A.

Here we compare two IGCM life cycles, referred to as LC1 and LC2 by Thorncroft et al. (1993), and distinguished by the basic state (see their Figs. 3(a) and 3(b)). The LC1 basic state was also used for the simulations of ABHP, and is a balanced, zonally-symmetric configuration designed to be representative of winter conditions over an ocean basin (Simmons and Hoskins 1980; cf. Valdes and Hoskins 1988). The LC2 basic state differs from that of LC1 only through the addition of a barotropic component to the zonal wind that contributes a cyclonic shear. As argued by Hoskins and West (1979), this results in a more pronounced warm front. The LC2 baroclinic wave also decays rather slowly, in marked contrast to the LC1 wave for which growth and decay rates are comparable. Thus, the LC2 life cycle provides a useful test of the robustness of the ABHP picture.

Running the LC2 life cycle with a boundary layer parameterization introduces a complication that was not relevant to previous IGCM studies of baroclinic waves. This is because the LC2 basic state has non-zero wind at the surface, and so the action of the parameterization may damage the

¹This study attempts to establish basic dynamical mechanisms and their range of validity. While the use of other parameterizations of the boundary layer may be an interesting topic for future investigation, one would not expect see $\mathcal{O}(1)$ changes in the results.

basic state itself. A similar issue arises when including a parameterization of turbulent heat fluxes in both the LC1 and LC2 life cycles. One could attempt to compensate for such effects by imposing additional tendencies in the equation set that would cancel the action of the parameterization on the basic state. However, we do not consider such a strategy to be necessary in practice. Table 1 shows the energy losses incurred in 20 day model integrations for which the initial state is the basic state (i.e., there is no normal mode perturbation). In this Table, we have introduced a convenient labelling scheme for the model runs, which will be used in the remainder of this paper. The subscript 0 denotes a run without the boundary layer parameterization, whereas m and h indicate the inclusion of turbulent momentum and heat fluxes respectively. The identifiers also include a letter and a number: the letter indicates the presence (P) or absence (A) of the baroclinic wave and the number refers to the basic state.

[Table 1 about here.]

Note first that the energy loss from hyperdiffusion (in runs A1₀ and A2₀) is negligible. Although there are indeed some losses caused by the boundary layer parameterization, particularly for the LC2 state, these remain small on the scale of the basic state. Importantly, the losses are considerably weaker than the eddy energies produced when the normal mode is added.

3. Mechanisms of PV Generation

The IGCM simulations are dry so that the free troposphere is frictionless and adiabatic. Numerical PV generation is modest (ABHP) and therefore significant material changes to PV can only occur because of the parameterized turbulent momentum and heat fluxes. Following both Cooper et al. (1992) and ABHP, in this section we use a simplified model of the boundary layer in order to focus

the discussion on the key physical processes capable of producing such changes to the PV.

Letting square brackets denote a vertical average over boundary layer depth h , the PV budget for the boundary layer may be written (see ABHP) as

$$\frac{\partial[P]}{\partial t} + \nabla_H \cdot [\mathbf{v}_H P] = [G] - \frac{w_h P_h}{h}. \quad (1)$$

where P is the potential vorticity and G its generation (defined in Eq. 2). The subscript H has been used to refer to horizontal components, while a subscript h denotes evaluation at $z = h$. On the left-hand-side of Eq. 1, the averaged PV is acted upon by the natural generalization of the advective derivative for a vertically-averaged field. The right-hand-side consists of the PV fluxed from the boundary layer into the free troposphere (second term), along with the averaged local PV generation. In writing the above budget, we have neglected some small terms dependent upon density variations within the boundary layer or on derivatives of the boundary layer height.

From the equations of motion, instantaneous, local PV production is given by (Hoskins et al. 1985)

$$\frac{DP}{Dt} \equiv G = \frac{1}{\rho} \left(\nabla \times \mathbf{F} \cdot \nabla \theta + \zeta \cdot \nabla \frac{D\theta}{Dt} \right). \quad (2)$$

where \mathbf{F} is the frictional force and other symbols have their traditional meteorological meanings. It is convenient to decompose both the frictional and diabatic pieces into contributions from the horizontal and vertical components of the relevant dot products. Then, scaling the frictional force and diabatic heating with the corresponding surface values (Cooper et al. 1992), so that

$$\mathbf{F} = \frac{\tau_s}{\rho} \frac{\partial S}{\partial z} \quad ; \quad \frac{D\theta}{Dt} = -H_s \frac{\partial R}{\partial z}, \quad (3)$$

produces

$$\begin{aligned}
[G] = & \hat{\mathbf{k}} \cdot \nabla \times \boldsymbol{\tau}_s \left[\frac{1}{\rho^2} \frac{\partial \theta}{\partial z} \frac{\partial S}{\partial z} \right] + \hat{\mathbf{k}} \times \boldsymbol{\tau}_s \cdot \left[\frac{1}{\rho^2} \nabla_H \theta \frac{\partial^2 S}{\partial z^2} \right] - H_s \left[\frac{1}{\rho} \zeta_z \frac{\partial^2 R}{\partial z^2} \right] \\
& - \nabla_H H_s \cdot \left[\frac{1}{\rho} \zeta_H \frac{\partial R}{\partial z} \right].
\end{aligned} \tag{4}$$

where we have again neglected some small terms (ABHP). The physical interpretation of the above equation is facilitated by assuming a linear decrease of S and R , the stress and heat flux profiles, across the boundary layer depth right down to the surface. (As in Cooper et al. (1992); ABHP. See Fig. 3.3 of Garratt (1994) for an example of data in support of the approximation.) This allows one to perform the averaging analytically. The generation of boundary-layer PV can then be assigned to four simple, distinct processes:

$$\begin{aligned}
[G] = & \frac{1}{\rho h^2} \left(-f \Delta \theta w_E + \frac{1}{\rho} \hat{\mathbf{k}} \times \boldsymbol{\tau}_s \cdot (\nabla_H \theta)_h - H_s \zeta_z(z = h) \right. \\
& \left. + \nabla H_s \cdot \hat{\mathbf{k}} \times (\mathbf{v}_h - h[\nabla w]) \right),
\end{aligned} \tag{5}$$

where w_E is the Ekman pumping velocity and $\Delta \theta = \theta(h_+) - \theta(0_+)$ is the potential temperature difference across the boundary layer ($\theta(h_+)$ being just above any boundary layer inversion and $\theta(0_+)$ the air temperature just above the surface). w_E is defined as in Sec. 4 of Pedlosky (1987),

$$w_E = \frac{\hat{\mathbf{k}} \cdot \nabla \times \boldsymbol{\tau}_s}{\rho f} \tag{6}$$

The first two terms appearing on the right-hand-side of Eq. 5 correspond to the barotropic and baroclinic frictional mechanisms discussed by ABHP. The first (barotropic) term is the analogue in PV terms of the Ekman pumping mechanism for the spindown of a barotropic vortex, while the second (baroclinic) term is governed by the relative orientation of the surface and thermal winds:

specifically, it is proportional to their negative dot product.

The direct effects of turbulent heat fluxes are given by the third term, proportional to the surface heat flux (H_s), and the fourth term, proportional to its gradient². The third term is manifestly barotropic, whereas the fourth term can be thought of as quasi-baroclinic. If one substitutes the bulk aerodynamic formula for the surface heat flux into the fourth term, it is immediately apparent that the term will survive in the absence of baroclinicity, owing to gradients of both the Stanton number, C_H , and the lowest model-level wind speed, $|\mathbf{v}_1|$. However, direct evaluation of simulation results shows that the most important contribution to the fourth term comes from the action of the gradient operator on the surface-layer stability factor³, $T_1 - T_{\text{surface}}$. Even this baroclinic contribution to the fourth term would not be expected to be important, since large discrepancies between near-surface and surface baroclinicities are unusual. Indeed, we have checked that the fourth term in Eq. 5 is small throughout both the LC1 and LC2 life cycles.

In contrast, we have found that the third term in Eq. 5 can be significant. Its physical origin is easily understood: heating of near-surface air reduces the low-level static stability, thereby (assuming a positive absolute vorticity) reducing the PV. Assuming the initial near-surface air temperature is in equilibrium with the temperature of the surface itself, one therefore expects to find positive PV generation in the warm sector of a northern-hemisphere mid-latitude cyclone, along with reduced PV behind the cold front.

²The small contribution to this term arising from the averaged horizontal gradient of vertical velocity was omitted by Cooper et al. (1992).

³This is analogous to the observation of ABHP that the most important contribution to the first term in Eq. 5 (which is proportional to $\hat{\mathbf{k}} \cdot \nabla \times \boldsymbol{\tau}_s$) comes from the action of the curl operator on the factor \mathbf{v}_1 in the bulk aerodynamic formula for the surface wind stress.

4. Life Cycles

Before examining the low-level evolution of the simulated baroclinic waves, we provide in this section an overview of life cycle behaviour with the parameterized boundary layer included. For the LC1 life cycle, ABHP found that friction dampened the baroclinic wave and introduced a delay of around one day in its evolution. Figure 2 shows that similar behavior occurs when friction is introduced into the LC2 life cycle, albeit with a longer delay of about three days in the peak energy. Turbulent heat fluxes have little effect on phase, but do reduce the energy content of the baroclinic wave. Associated with these effects on eddy kinetic energy are corresponding effects in other measures of wave strength such as the pressure perturbation and relative vorticity maximum (not shown).

[Figure 2 about here.]

Since the baroclinic waves in different simulations evolve at different rates it would not be appropriate to compare results between simulations at particular, fixed times. Instead, we prefer to make comparisons at roughly equivalent stages of the life cycles. It is convenient therefore to define times of early, mid- and later growth, at which the eddy kinetic energy has reached, respectively, 5, 33 and 67% of its peak value. These times are listed in days for each model run in Table 2. We also define an early decay time, at which the eddy kinetic energy has fallen to 75% of its peak value.

[Table 2 about here.]

Figure 2 shows a marked contrast in the barotropic decay of the LC1 and LC2 life cycles. This was mentioned in Sec. 2 and can be understood in terms of the upper-level PV evolution, bearing in mind that the jet location governs the relative contributions of cyclonic and anti-cyclonic shear

to the maintenance or destruction of PV structures (Thorncroft et al. 1993; Methven et al. 2005). In Fig. 3 we show, for the early decay stage, the potential temperature and winds on the dynamical tropopause surface, $PV = 2PVU$. In the LC1 case, energy growth and decay rates are comparable, and each is reduced by the inclusion of a parameterized boundary layer. Upper-level momentum fluxes act to displace the jet northwards (Simmons and Hoskins 1978). Some limited cyclonic turning of the potential temperature contours occurs on the dynamical tropopause during wave development. However, this is followed by trough thinning owing to anti-cyclonic turning south of the displaced jet (Fig. 3(a)). The thinning leads to decay of the upper-level anomaly.

[Figure 3 about here.]

The LC2 life cycle $P2_0$ (without any boundary layer parameterization) evolves quite differently from LC1, being marked by a much weaker rate of decay. In this case a slight southern displacement of the jet combined with the limited meridional extent of the developing upper-level anomaly means that cyclonic wrap-up dominates the evolution of the mature anomaly. A highly-persistent vortex is produced (Fig. 3(b)) which remains prominent at the end of the simulation, after 20 days.

When friction is included in LC2 (Fig. 3(c)), the behavior is intermediate between the two types just described. A long-lived vortex is formed, as in LC2 without friction, but a modest northerly jet displacement as the wave approaches maturity now means that there is also significant anti-cyclonic turning on the southern flank of the anomaly. Thus, anomalous potential temperature is extracted from the vortex, producing a streamer to the south. Steady erosion of the vortex means that it is barely discernible after 20 days (not shown).

5. Low-Level Fronts

An important aspect of the ABHP picture is baroclinic frictional generation of PV, which is proportional to the potential temperature gradient at the top of the boundary layer (Eq. 5). It is important therefore to consider the impact of the parameterized boundary layer on the evolution of low-level fronts in these simulations. There is a considerable literature discussing in more detail the effects of boundary layer processes on frontogenesis, including numerical (e.g. Hines and Mechoso 1993; Kuo and Low-Nam 1994; Thompson and Williams 1997; Rotunno et al. 1998; Bryan and Fritsch 2000) and analytical (e.g. Blumen 1980; Snyder 1998) studies.

We base our discussion on the runs $P1_m$ and $P2_m$, which have a parameterization of turbulent momentum fluxes, but not of turbulent heat fluxes. We will describe the impact of turbulent heat fluxes towards the end of the section. Figure 4 shows the low-level potential temperature in the mid-growth stage of $P1_m$ and $P2_m$. The LC1 life cycle at this stage (Fig. 4(a)) is characterised by a pronounced cold front which wraps around the anti-cyclone, along with a bent-back warm front. At later times, the warm frontal gradient slackens, leaving the cold front as the dominant feature. Further development also draws warm sector air towards the low, forming a seclusion.

[Figure 4 about here.]

As mentioned in Sec. 2, the barotropic shear added to the LC2 basic state leads to a more marked warm front. This is the dominant feature in the early growth stage (not shown), but during the transition to the mid-growth stage the cold front intensifies rapidly, such that it is of comparable strength in Fig. 4(b).

Examining sequences of such plots for both LC1 and LC2 with and without friction (not shown) reveals that the inclusion of friction dampens the low-level temperature wave, with the main effects

occurring in the region of the warm front. For example, in both the LC1 and LC2 life cycles the strength of the cold front at the mid-growth stage is similar to that in the corresponding run without any boundary layer parameterization. However, at the same stage, the warm front is clearly weaker with friction included.

Retardation of low-level warm advection is particularly marked in the development of the LC2 life cycle. By the later growth stage, a seclusion of warm air has formed in the LC2 simulation without boundary layer parameterization (Fig. 5(a)). A distinct bent-back warm front can also be seen, which is largely absent from the LC2 simulation with friction included (Fig. 5(b)). These observations are consistent with the results of Kuo and Low-Nam (1994), who discussed the role of friction in the process of seclusion.

[Figure 5 about here.]

The asymmetric effect of friction on cold and warm fronts also occurs in simulations of baroclinic waves with an Ekman boundary condition (Rotunno et al. 1998). During wave growth, Ekman pumping is stronger in the vicinity of the warm front, since this is formed closer to the low center⁴. The pumping cools the boundary layer, arresting the system-relative progression of warm sector air. The present results support this interpretation, the Ekman pumping velocity being plotted in Fig. 4.

In the simulations performed here, the sea surface temperature depends only on latitude. Therefore, surface heat fluxes act to cool or warm near-surface air which has made a meridional excursion from its original position. As a result, near-surface fronts are weaker in the model runs that include such fluxes. Although one might expect this to lead to a reduction in the relative importance of baroclinic frictional generation of PV, the slackening of frontal gradients is diminished

⁴Consistent with the surface divergence field in a recent composite of observed mid-latitude cyclones (Fig. 3b of Field and Wood 2006), Ekman pumping occurs at and to the east of the low center.

with height (see Fig. 13 for an example) (Thompson and Williams 1997) and is rather modest towards the top of the boundary layer.

6. Boundary Layer PV in LC2

We are now in a position to investigate the sensitivities of frictional PV generation, and its subsequent transport, to the low-level frontal structures seen in the LC1 and LC2 life cycles. We consider the runs $P1_m$ and $P2_m$, deferring to Sec. 7 a discussion of the effects of turbulent heat fluxes. PV generation terms are computed from Eq. 5, with the boundary layer top being taken as the model level $\sigma = 0.92$. As discussed by ABHP, this simple approach is reasonable given the approximations made in obtaining Eq. 5 and is sufficient for our present purposes.

The detailed evolution of low-level PV in $P1_m$ was described by ABHP. During growth of the baroclinic wave, the inclusion of friction leads to the development of two distinct PV anomalies: (i) a negative anomaly at the base of the boundary layer just above the low center; and, (ii) a thin, positive anomaly just above the boundary layer. The negative anomaly is generated by the barotropic frictional term, whilst the positive anomaly develops from PV that is generated by the baroclinic frictional term in an arc extending from just ahead of the leading edge of the cold front to the vicinity of the bent-back warm front. The generated positive PV is transported out of the boundary layer within the large-scale ascending flow of the warm conveyor belt and is then carried westwards over the low center.

A notable feature of the LC2 life cycle with friction included is that PV generation due to the baroclinic frictional mechanism is active at the outset of the simulation. (The basic state contains zonal flow at the surface and a thermal westerly wind.) The result at the very earliest times is a near-surface strip of anomalous PV between $\sim 40^\circ\text{N}$ to 55°N . By the early growth stage, as the

wave starts to develop, the anomalous PV becomes concentrated along the nascent warm front (Fig. 6). Figure 7 shows the baroclinic frictional PV generation (second term in Eq. 5), with a source area that is consistent with the schematic diagram of Fig. 1. At the early growth stage, vertical velocities are small and so the generated PV remains confined to the lowest one or two model levels. The barotropic frictional mechanism is just becoming active (not shown), and serves as a partial counter to the baroclinic PV generation, along the southern and western flanks of the structure seen in Fig. 7.

[Figure 6 about here.]

[Figure 7 about here.]

By the mid-growth stage of $P2_m$, the baroclinic wave has developed a mesoscale flow capable of transporting the generated positive PV towards the top of the boundary layer and into the free troposphere. Low-level ascending flow at this time is dominated by rearward flow on the cold side of the warm front: i.e., it takes the form of a cold-conveyor belt (Carlson 1980; Browning 1999). Figure 8(a) shows the ascent at the top of the boundary layer. The low-level PV can be seen in Fig. 9. The generated PV ascends and moves westwards within the mesoscale flow to form a positive anomaly above the low center at the top of the boundary layer (Fig. 9(c)). This is very much reminiscent of the positive anomaly found in the LC1 case by ABHP. The main difference in the PV generation is that this occurs in LC2 almost exclusively at the warm front, whereas in LC1, more modest generation towards the warm front is supplemented by PV generation on the warm flank of the cold front. There is a significant difference in the subsequent transport to the free troposphere, but in both cases, the generated PV is favorably positioned to ascend within the relevant conveyor belt flow.

[Figure 8 about here.]

[Figure 9 about here.]

Another aspect of the mid-growth stage of $P2_m$ is that, as shown in Fig. 10, the regions of frictional barotropic and baroclinic generation of PV start to become spatially distinct. Although there remains significant cancellation between the terms, there is also sufficient displacement for a region of net PV destruction to become established at and close to the surface low center. As in the LC1 case, PV destruction in such a position produces a negative PV anomaly in the lower part of the boundary layer, above the low center. The anomaly can be seen at the later growth stage in Fig. 11.

There is a transition in the frontal structure of $P2_m$ (Sec. 5) such that the cold front becomes prominent by the later growth stage. Related is a transition in the nature of the low-level ascending flow, which is dominated by a cold-conveyor belt pattern in the mid-growth stage (Fig. 8(a)) but is more typical of a warm-conveyor belt (Fig. 8(b)) by the later growth stage. During the transition, baroclinic frictional generation of PV becomes less associated with the remnants of the warm front and more and more with the warm flank of the cold front. The overall result is that the generation and transport of positive anomalous PV becomes increasingly similar to that in the LC1 case (Fig. 9)⁵.

[Figure 10 about here.]

[Figure 11 about here.]

⁵The reader who wishes to make a direct comparison is invited to consider Fig. 11 along with Fig. 5 from ABHP and Fig. 9 here.

7. Action of Turbulent Heat Fluxes

The inclusion of turbulent heat fluxes in the boundary layer parameterization is potentially important for two reasons. First, the fluxes may modify the action of frictional processes; for instance, by altering the boundary-layer stability (affecting the barotropic frictional PV generation: see Eq. 5) or by weakening frontal gradients (affecting the baroclinic frictional generation: see Sec. 5). Second, turbulent heat fluxes may introduce direct effects of their own (Sec. 3).

7a. *Turbulent Heat Fluxes in LC1*

We begin by comparing the LC1 life cycle runs $P1_m$ and $P1_{mh}$, respectively without and with parameterized turbulent heat fluxes. The effects of such fluxes on the LC2 life cycle will then be described.

Figure 12 shows PV generation terms computed for $P1_{mh}$ at its early growth stage⁶. The frictional generation terms (Fig. 12(a),(b)) are rather similar to those found in $P1_m$, although the baroclinic generation term is a little weaker, reflecting the weaker fronts (Sec. 5). More significant is the introduction of the barotropic heat-flux term (third term in Eq. 5, shown in Fig. 12(c)). As anticipated in Sec. 3 this is positive where warm air has been advected northwards; i.e., in the warm sector, particularly towards the developing warm front. PV destruction also occurs, where cold air is advected equatorwards, but this is more closely associated with the high rather than low pressure part of the baroclinic wave.

[Figure 12 about here.]

These remarks about the effects of turbulent heat fluxes on PV generation at the early growth

⁶The reader who wishes to make their own comparison with corresponding results from the $P1_m$ run is referred to Fig. 9 of ABHP.

stage also hold true during later development, and are able to explain the effects on low-level PV structure. The main PV structures seen (in Fig. 13) at the mid-growth stage of $P1_{mh}$ are⁷:

1. negative anomalous PV that extends through the boundary layer (centered at $\sim 20^\circ\text{W } 50^\circ\text{N}$ in Fig. 13(a)). This is generated by the barotropic heat-flux term and is associated with the high pressure part of the wave;
2. a negative PV anomaly at the base of the boundary layer upstream of the low (at $\sim 60^\circ\text{W } 55^\circ\text{N}$ in Fig. 13(a)). This is generated by the barotropic frictional term; and,
3. a strong, positive PV anomaly, with the PV being generated near the crest of the temperature wave close to the surface (at $\sim 40^\circ\text{W } 55^\circ\text{N}$ in Fig. 13(a)) and then transported through the boundary layer by the warm conveyor belt flow. The generation occurs due to the combined action of the baroclinic frictional and barotropic heat-flux terms, albeit partially offset by cancellation with the barotropic frictional term.

The positive PV anomaly evolves similarly to the corresponding structure in the run $P1_m$ without turbulent heat fluxes. PV generation continues to occur ahead of the northern part of the cold front, particularly where the warm sector air approaches the warm front. With turbulent heat fluxes included, such generation is associated with a weaker baroclinic frictional term but near-surface cooling produces significant generation from the barotropic heat-flux term. The generated PV is transported out of the boundary layer within the cyclonic W2 branch of the warm-conveyor belt to form an anomaly above the low center.

[Figure 13 about here.]

⁷The reader who wishes to make their own comparison with corresponding results from the $P1_m$ run is referred to Fig. 5 of ABHP.

7b. *Turbulent Heat Fluxes in LC2*

We now turn to the LC2 life cycle with the full boundary layer parameterization, run $P2_{mh}$. Recall that in the run $P2_m$, without turbulent heat fluxes, positive PV was generated due to the baroclinic frictional mechanism from the very beginning of the simulation. In $P2_{mh}$, such PV generation again occurs, but the anomaly at the early growth stage is considerably smaller and weaker than that shown in Fig. 6. Partly this is because the baroclinic frictional PV generation is somewhat reduced, owing to weaker thermal gradients in the developing wave. More important, however, is that the barotropic heat-flux term is also active at very early times, and is at those times predominantly negative (the northerly component of meridional flow being more readily established).

From the early growth stage onwards, however, the effects of turbulent heat fluxes in the LC2 life cycle are similar in character to those in LC1. This is illustrated by Fig. 14, showing the PV generation terms at the early growth stage. It may be compared to the corresponding plot for the $P2_m$ run in Fig. 7. The baroclinic frictional term has been somewhat weakened over the warm front (Fig. 14(b)), but this is partially compensated by modest PV generation from the barotropic heat-flux term (Fig. 14(c)). As in $P2_m$, the PV generated to the east and north-east of the low center is transported by the cold-conveyor belt, giving rise to a well-defined positive PV anomaly at the mid-growth stage. Values of PV occurring in the anomaly in $P2_{mh}$ are smaller than those in its counterpart in $P2_m$, due to the weaker net generation of positive PV at the beginning of the run.

[Figure 14 about here.]

By the mid-growth stage of $P2_m$, barotropic frictional destruction of PV becomes spatially distinct from baroclinic frictional generation, so that a negative PV anomaly can be seen at the later growth stage (Sec. 6). The negative anomaly is more immediately apparent in plots of the

low-level PV from the $P2_{mh}$ run (not shown), since it is no longer superimposed on significant background positive PV generated at the earliest times.

8. Static Stability

In Secs. 6 and 7 we have discussed low-level PV evolution during the growth of simulated baroclinic waves. A recurring feature is a positive PV anomaly located towards the top and just above the boundary layer over the low center. For the LC1 run $P1_m$, ABHP stressed that the PV anomaly is thin and so associated with anomalously high static-stability. This point is crucial for their explanation of the damping effect of friction upon the growing baroclinic wave: the increased stability reduces the coupling between the surface and the interior anomaly in the wave. Here we test whether the same interpretation holds for the other life cycle simulations.

Figure 15 shows the zonal-mean static stability in both the LC1 and LC2 life cycles, using the full boundary layer parameterization. Results for LC1 at the later growth stage appear in Fig. 15(a). One feature to note is a region of high stability centered at $\sim 40^\circ\text{N}$ and $\sigma \sim 0.8$. This is due to the stratospheric intrusion. There are also three features of the zonal-mean stability which are signatures of the three low-level PV anomalies described previously (Sec. 7). First, a region of low boundary-layer stability is centered to the south of the low at $\sim 40^\circ\text{N}$, associated with the negative anomaly generated by the barotropic heat-flux mechanism. Second, there is low stability at the base of the boundary layer over the low (at $\sim 60^\circ\text{N}$), associated with the barotropic frictional mechanism (i.e., with Ekman pumping). And, third, and most prominently, there is indeed a high-stability feature present at the latitude of the low and occupying the upper part of the boundary layer and the lower troposphere (between $\sigma \sim 0.98$ and 0.85). Similar features are also observed for the LC2 life cycle in both its mid-growth (Fig. 15(b)) and later-growth (Fig. 15(c)) stages, despite the

changes that take place during this time in the frontal configuration (Sec. 5), and consequently also in the processes of PV generation and transport (Sec. 6).

[Figure 15 about here.]

9. Variation of Roughness Length

Varying the surface roughness, there are competing effects on the mechanisms for PV generation. For instance, while increased roughness leads to increased stresses, it also dampens the low-level temperature wave so that the net effect on PV generation by the baroclinic frictional and barotropic heat-flux terms is unclear. Although important effects may occur over a land surface (e.g., since warm fronts are disproportionately weakened, (Hines and Mechoso 1993)), we have checked that changing roughness lengths by up to an order of magnitude in our simulations is insufficient to change the basic processes through which the marine boundary layer affects baroclinic wave dynamics. The negative PV anomaly associated with Ekman pumping is perceptible a little earlier with increased roughness but its structure and strength are not systematically altered. The positive PV anomaly also remains of very similar strength, although it is transported a little further into the troposphere with increasing roughness, with the result that the associated static-stability anomaly is displaced upwards.

The qualitative change in behavior of the mature LC2 life cycle, from persistent to gradually-decaying vortex (Sec. 4), requires only weak levels of surface roughness, occurring for $z_0 \gtrsim 10^{-6}\text{m}$ with the full boundary layer parameterization or for $z_0 \gtrsim 10^{-5}\text{m}$ with parameterized turbulent momentum fluxes only.

10. Conclusions

A simple parameterization of the turbulent fluxes of heat and momentum has been included in an idealized three-dimensional baroclinic life-cycle model. Following previous studies (e.g., Cooper et al. 1992; Stoelinga 1996; Adamson et al. 2006) the resulting modifications to baroclinic-wave dynamics have been examined in a potential-vorticity framework. Some previous studies have highlighted the net frictional generation of positive PV, in marked contrast to the PV destruction associated with the Ekman pumping mechanism. Anomalous positive PV is able to dampen baroclinic wave development because it is associated with enhanced static stability in the lower troposphere, reducing the coupling of upper and lower-level waves (Stoelinga 1996; Adamson et al. 2006).

The focus of this study has been the impact of turbulent heat fluxes on the wave damping, and sensitivities to frontal structure and mesoscale flow patterns. We find that the essential features of the damping are robust, at least for values of roughness found over the oceans. Baroclinic frictional generation of PV occurs in the eastern and north-eastern sector of the low, as argued by Adamson et al. (2006) (see Fig. 1). Turbulent heat fluxes weaken low-level fronts and somewhat reduce this generation, an effect which is at least partially offset by direct PV generation due to a barotropic heat-flux mechanism. Turbulent heat fluxes also act to remove PV in the cold-sector air to the west, although this effect appears to be more closely associated with the high pressure part of the baroclinic waves simulated here.

Production of a thin, positive PV anomaly above the low center, towards the top of the boundary layer and in the lower part of the troposphere, occurs regardless of frontal structure and mesoscale flow patterns. Either a warm or a cold front may be prominent in the low-level temperature wave, with the LC2 life cycle evolving from the former to the latter arrangement. In either case, however,

positive PV is generated in a location that is favorable for transport within an appropriate conveyor belt flow. Although the boundary layer circulation associated with Ekman pumping may be a significant factor in moulding a PV anomaly of the required shape (Xu et al. 1988), the direct effect of Ekman pumping in spinning-down low-level vorticity would appear to be less important than the baroclinic frictional PV generation and its subsequent transport.

While the wave damping mechanism described by Adamson et al. (2006) is robust for dry baroclinic waves, it remains to be seen whether it plays a similar role within real cyclones, in which lower-tropospheric flows are modified by moist dynamics. Aspects of the results of Davis et al. (1993) and Stoelinga (1996) are encouraging in this regard, as are some diagnostics computed for real systems by Field (personal communication) and Simon (personal communication). We intend to report shortly on our own analysis of some real cases.

Acknowledgement R. Plant acknowledges funding from the UWERN programme, supported by NERC.

A. Boundary Layer Parameterization

The boundary layer scheme implemented into the IGCM parameterizes vertical fluxes of both momentum and sensible heat. A general description of the scheme is given by ABHP, along with details of the calculations for momentum fluxes. Some additional expressions are required in order to calculate the turbulent heat fluxes and these are presented here.

A bulk aerodynamic formula is used for the surface heat flux. Hence, the neutral Stanton number, C_H , depends upon roughness lengths for heat and momentum, which are taken to be identical. Variation of the Stanton number with surface layer stability is determined by Monin-Obukhov similarity theory, using flux profiles from Arya (1988),

$$\phi_h = \begin{cases} 1 + 5z/L_{MO} & \text{for } z/L_{MO} > 0 \\ (1 - 15z/L_{MO})^{-1/2} & \text{for } z/L_{MO} < 0 \end{cases} \quad (7)$$

where ϕ_h is the non-dimensionalized profile and L_{MO} the Monin-Obukhov length.

Above the lowest model level, a mixing length scheme based on Louis (1979) is used, with the turbulent diffusion coefficient for heat, K_h , written as

$$K_h = l_m^2 \left| \frac{\partial \mathbf{v}}{\partial z} \right| f_h(\text{Ri}), \quad (8)$$

Here the mixing length l_m is obtained from a modified Blackadar formula (ABHP) and the function f_h of Richardson number accounts for the effects of stability. Specifically,

$$f_h = \begin{cases} \frac{1}{1 + 2b\text{Ri}(1 + d\text{Ri})^{-1/2}} & \text{for } \text{Ri} \geq 0 \\ 1 - \frac{3b\text{Ri}}{1 + 3bc\sqrt{-\text{Ri}}(l_m/z)^2 3^{-3/2}} & \text{for } \text{Ri} < 0 \end{cases} \quad (9)$$

where $b = c = 5$ (Louis et al. 1982; ECMWF Research Department 1991) and $d = 1$ (Viterbo et al. 1999; ECMWF Research Department 2002).

References

- Adamson, D. S., S. E. Belcher, B. J. Hoskins, and R. S. Plant, 2006: Boundary-layer friction in midlatitude cyclones. *Q. J. R. Meteorol. Soc.*, **132**, 101–124.
- Ahmadi-Givi, F., G. C. Craig, and R. S. Plant, 2004: The dynamics of a midlatitude cyclone with very strong latent-heat release. *Q. J. R. Meteorol. Soc.*, **130**, 295–323.
- Anthes, R. A. and D. Keyser, 1979: Tests of a fine-mesh model over Europe and the United States. *Mon. Wea. Rev.*, **107**, 963–984.
- Arya, S. P., 1988: *Introduction to Micrometeorology*. Academic Press.
- Blumen, W., 1980: A comparison between the Hoskins–Bretherton model of frontogenesis and the analysis of an intense surface frontal zone. *J. Atmos. Sci.*, **37**, 64–76.
- Browning, K. A., 1999: Mesoscale aspects of extratropical cyclones: An observational perspective. *The Life Cycles of Extratropical Cyclones*, M. A. Shapiro and S. Gronas, eds., Amer. Met. Soc., 265–283.
- Bryan, G. H. and J. M. Fritsch, 2000: Diabatically driven discrete propagation of surface fronts: A numerical analysis. *J. Atmos. Sci.*, **57**, 2061–2079.
- Carlson, T. N., 1980: Airflow through mid-latitude cyclones and the comma cloud pattern. *Mon. Wea. Rev.*, **108**, 1498–1509.
- Cooper, I. M., A. J. Thorpe, and C. H. Bishop, 1992: The role of diffusive effects on potential vorticity in fronts. *Q. J. R. Meteorol. Soc.*, **118**, 629–647.

- Davis, C. A., M. T. Stoelinga, and Y.-H. Kuo, 1993: The integrated effect of condensation in numerical simulations of extratropical cyclogenesis. *Mon. Wea. Rev.*, **121**, 2309–2330.
- ECMWF Research Department, 1991: *ECMWF Forecast Model: Physical Parameterization*. 3rd edition, Research Manual 3.
- 2002: IFS Documentation. Part IV: Physical processes (CY25R1). Technical report, ECMWF, P. W. White (Ed.).
- Farrell, B. F., 1986: Transient growth of damped baroclinic waves. *J. Atmos. Sci.*, **42**, 2718–2727.
- 1989: Unstable baroclinic modes damped by Ekman dissipation. *J. Atmos. Sci.*, **46**, 397–401.
- Field, P. R. and R. Wood, 2006: Precipitation and cloud structure in midlatitude cyclones. Submitted.
- Garratt, J. R., 1994: *The Atmospheric Boundary Layer*. Cambridge University Press.
- Hines, K. M. and C. R. Mechoso, 1993: Influence of surface drag on the evolution of fronts. *Mon. Wea. Rev.*, **121**, 1152–1175.
- Holton, J. R., 1992: *An Introduction to Dynamic Meteorology*. Academic Press, 3rd edition.
- Hoskins, B. J., M. E. McIntyre, and A. W. Robertson, 1985: On the use and significance of isentropic potential vorticity maps. *Q. J. R. Meteorol. Soc.*, **111**, 877–946.
- Hoskins, B. J. and A. J. Simmons, 1975: A multi-layer spectral model and the semi-implicit method. *Q. J. R. Meteorol. Soc.*, **101**, 637–655.
- Hoskins, B. J. and N. V. West, 1979: Baroclinic waves and frontogenesis. Part II: Uniform potential vorticity jet flows - cold and warm fronts. *J. Atmos. Sci.*, **36**, 1663–1680.

- Kuo, Y.-H. and S. Low-Nam, 1994: Effects of surface friction on the thermal structure of an extratropical cyclone. *Proc. Int. Symp. on the Life Cycles of Extratropical Cyclones*, S. Gronas and M. A. Shapiro, eds., Geophysical Institute, University of Bergen, Norway, volume III, 129–134.
- Louis, J. F., 1979: A parametric model of vertical eddy fluxes in the atmosphere. *Bound. Lay. Meteorol.*, **17**, 187–202.
- Louis, J. F., M. Tiedtke, and J. F. Geleyn, 1982: A short history of the operational PBL — Parameterization at ECMWF. *Workshop on Planetary Boundary Layer Parameterization*, **17**, 59–79.
- Methven, J., B. J. Hoskins, E. Heifetz, and C. H. Bishop, 2005: The counter-propagating Rossby-wave perspective on baroclinic instability. Part IV: Nonlinear life cycles. *Q. J. R. Meteorol. Soc.*, **131**, 1425–1440.
- Moore, R. W. and M. T. Montgomery, 2004: Reexamining the dynamics of short-scale, diabatic Rossby waves and their role in midlatitude moist cyclogenesis. *J. Atmos. Sci.*, **61**, 754–768.
- Nakamura, N. and I. M. Held, 1989: Nonlinear equilibration of two-dimensional Eady waves. *J. Atmos. Sci.*, **46**, 3055–3064.
- Pedlosky, J., 1987: *Geophysical Fluid Dynamics*. Springer Verlag, 2nd edition.
- Reed, R. J., G. A. Grell, and Y.-H. Kuo, 1992: The ERICA IOP 5 storm. Part II: Sensitivity tests and further diagnosis based on model output. *Mon. Wea. Rev.*, **121**, 1595–1612.
- Rotunno, R., W. C. Skamarock, and C. Snyder, 1998: Effects of surface drag on fronts within numerically simulated baroclinic waves. *J. Atmos. Sci.*, **55**, 2119–2129.

- Simmons, A. J. and B. J. Hoskins, 1978: The lifecycles of some nonlinear baroclinic waves. *J. Atmos. Sci.*, **35**, 414–432.
- 1980: Barotropic influences on the growth and decay of nonlinear baroclinic waves. *J. Atmos. Sci.*, **37**, 1679–1684.
- Snyder, C., 1998: Approximate dynamical equations for fronts modified by the planetary boundary layer. *J. Atmos. Sci.*, **55**, 777–787.
- Stoelinga, M. T., 1996: A potential vorticity-based study of the role of diabatic heating and friction in a numerically simulated baroclinic cyclone. *Mon. Wea. Rev.*, **124**, 849–874.
- Thompson, W. T. and R. T. Williams, 1997: Numerical simulations of maritime frontogenesis. *J. Atmos. Sci.*, **54**, 314–331.
- Thorncroft, C. D., B. J. Hoskins, and M. E. McIntyre, 1993: Two paradigms of baroclinic-wave life-cycle behaviour. *Q. J. R. Meteorol. Soc.*, **119**, 17–55.
- Uccellini, L. W., R. A. Petersen, P. J. Kocin, K. F. Brill, and J. J. Tuccillo, 1987: Synergistic interactions between an upper-level jet streak and diabatic processes that influence the development of a low-level jet and a secondary coastal cyclone. *Mon. Wea. Rev.*, **115**, 2227–2261.
- Valdes, P. J. and B. J. Hoskins, 1988: Baroclinic instability of the zonally averaged flow with boundary layer damping. *J. Atmos. Sci.*, **45**, 1584–1593.
- Viterbo, P., A. C. M. Beljaars, J.-H. Mahouf, and J. Teixeira, 1999: The representation of soil moisture freezing and its impact on the stable boundary layer. *Q. J. R. Meteorol. Soc.*, **125**, 2401–2426.

Xu, Q., W. Gu, and J. D. Gao, 1988: Baroclinic Eady waves and fronts. Part 1: Viscous semi-geostrophy and the impact of boundary conditions. *Mon. Wea. Rev.*, **55**, 3598–3615.

List of Figures

- 1 Schematic illustrating the baroclinic mechanism for the generation of PV due to friction in the linear phase of a growing baroclinic wave. L and H denote the surface low and high pressure centers, the arrowheads denote near-surface winds (v_s) and the long arrows denote the thermal wind (v_T). Shading indicates regions where $v_s \cdot v_T$ is large, darker shading being used for negative values (corresponding to positive PV generation). (After Adamson et al. 2006) 37
- 2 The domain-averaged eddy kinetic energy with and without parameterized turbulent fluxes of heat and momentum during (a) LC1 and (b) LC2 model life cycles. The labelling for each model run is described in full in Sec. 2. Subscript 0 denotes a run without the boundary layer parameterization, whereas m and h indicate the inclusion of turbulent momentum and heat fluxes respectively. 38
- 3 Potential temperature (5 K contour intervals) on the surface $PV = 2$ PVU in the early decay stage of runs (a) $P1_0$, (b) $P2_0$ and (c) $P2_m$. The elapsed time is nine days in (a), fifteen days in (b) and sixteen days in (c). Also shown are wind vectors on this surface, the scale for which appears in the top right. 39
- 4 Potential temperature (4 K contour intervals) on the surface $\sigma = 0.92$ in the mid-growth stage of the runs (a) $P1_m$, and (b) $P2_m$. The elapsed time is six days in (a) and seven days in (b). Also shown is the Ekman pumping velocity (0.2 cms^{-1} contour intervals for positive contours only; dashed). L and H denote the surface low and high pressure centers respectively. In (b) the highest pressure occurs to the north of the range of the figure. 40

- 5 Potential temperature (4 K contour intervals) on the surface $\sigma = 0.92$ in the later growth stage of: (a) P2₀ and (b) P2_m. The elapsed time is eight days in (a) and nine days in (b). L and H denote the surface low and high pressure centers respectively. In (b) the highest pressure occurs to the north of the range of the figure. 41
- 6 Potential temperature (4 K contour intervals) and PV (0.5 PVU contour intervals; dashed) in run P2_m in the early growth stage on the surface $\sigma = 0.955$. The elapsed time is five days. PV values larger than 1.5 PVU are shaded. L denotes the surface low pressure center. The highest pressure occurs to the north of the range of the figure. 42
- 7 Boundary layer-averaged frictional generation of PV (0.1 PVU/d contour intervals; dashed) from the baroclinic generation term in the early growth stage of the run P2_m. The elapsed time is five days. The zero contour has been suppressed and generation rates larger in magnitude than 0.1 PVU/d are shaded, a darker shading being used for positive values. Also shown is the potential temperature (4 K contour intervals) on the surface $\sigma = 0.92$. L denotes the surface low pressure center. The highest pressure occurs to the north of the range of the figure. 43
- 8 Ascent rate ω (0.02 Pas⁻¹ contour intervals, negative values only; dashed) and potential temperature (4 K contour intervals) on the surface $\sigma = 0.92$ in run P2_m in the (a) mid-growth and (b) later growth stages. The elapsed time is seven days in (a) and nine days in (b). L denotes the surface low pressure center. In both cases, the highest pressure occurs to the north of the range of the figure. 44

- 9 Potential temperature (4 K contour intervals) and PV (0.5 PVU contour intervals; dashed) in run $P2_m$ in the mid-growth stage on the surfaces (a) $\sigma = 0.98$, (b) $\sigma = 0.955$ and (c) $\sigma = 0.92$. The elapsed time is seven days. PV values larger than 2.5 PVU are shaded. L denotes the surface low pressure center. The highest pressure occurs to the north of the range of the figure. 45
- 10 Boundary layer-averaged frictional generation of PV (0.5 PVU/d contour intervals; dashed) in the mid-growth stage of run $P2_m$: (a) barotropic generation term and (b) baroclinic generation term. The elapsed time is seven days. The zero contour has been suppressed and generation rates larger in magnitude than 0.5 PVU/d are shaded, a darker shading being used for positive values. Also shown is the potential temperature (4 K contour intervals) on the surface $\sigma = 0.92$. L denotes the surface low pressure center. The highest pressure occurs to the north of the range of the figure. 46
- 11 Potential temperature (4 K contour intervals) and PV (0.5 PVU contour intervals; dashed) in run $P2_m$ in the later growth stage on the surfaces (a) $\sigma = 0.98$ and (b) $\sigma = 0.955$. The time elapsed is nine days. PV values larger than 2.5 PVU and smaller than -0.5 PVU are shaded, a darker shading being used in the former case. L denotes the surface low pressure center. The highest pressure occurs to the north of the range of the figure. 47

- 12 Boundary layer-averaged generation of PV (0.05 PVU/d contour intervals; dashed) in the early growth stage of run P1_{mh}: (a) barotropic frictional generation term, (b) baroclinic frictional generation term, (c) barotropic heat-flux generation term. The time elapsed is four days. The zero contour has been suppressed and generation rates larger in magnitude than 0.05 PVU/d are shaded, a darker shading being used for positive values. Also shown is the potential temperature (4 K contour intervals) on the surface $\sigma = 0.92$. L and H denote the surface low and high pressure centers. 48
- 13 Potential temperature (4 K contour intervals) and PV (0.5 PVU contour intervals; dashed) in run P1_{mh} in the mid-growth stage on the surfaces (a) $\sigma = 0.98$, (b) $\sigma = 0.955$ and (c) $\sigma = 0.92$. The time elapsed is six days. PV values larger than 1 PVU and smaller than 0 PVU are shaded, a darker shading being used in the former case. L and H denote the surface low and high pressure centers. 49
- 14 Boundary layer-averaged generation of PV (0.1 PVU/d contour intervals; dashed) in the early growth stage of run P2_{mh}: (a) barotropic frictional generation term, (b) baroclinic frictional generation term and (c) barotropic heat-flux generation term. The elapsed time is five days. The zero contour has been suppressed and generation rates larger in magnitude than 0.1 PVU/d are shaded, a darker shading being used for positive values. Also shown is the potential temperature (4 K contour intervals) on the surface $\sigma = 0.92$. L denotes the surface low pressure center. The highest pressure occurs to the north of the range of the figure. 50

15 Zonal-mean static stability ($5 \times 10^{-5} \text{ s}^{-2}$ contour interval) in the (a) later growth stage of run P1_{mh}, (b) mid-growth stage of run P2_{mh} and (c) later growth stage of run P2_{mh}. The elapsed time is seven days in (a), seven days in (b) and nine days in (c). Stabilities larger than $2.5 \times 10^{-4} \text{ s}^{-2}$ are shaded. 51

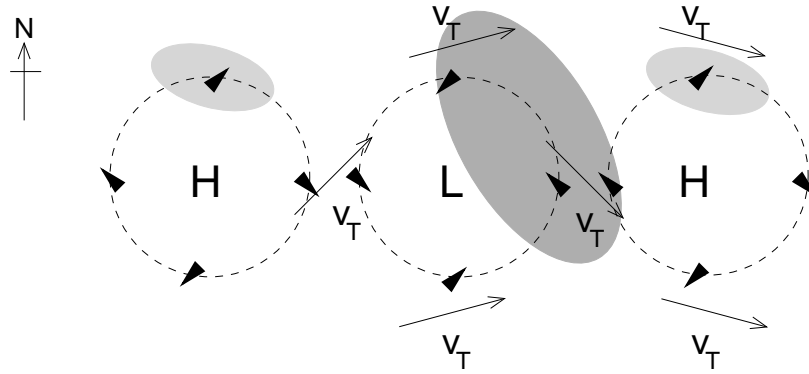


Figure 1: Schematic illustrating the baroclinic mechanism for the generation of PV due to friction in the linear phase of a growing baroclinic wave. L and H denote the surface low and high pressure centers, the arrowheads denote near-surface winds (v_s) and the long arrows denote the thermal wind (v_T). Shading indicates regions where $v_s \cdot v_T$ is large, darker shading being used for negative values (corresponding to positive PV generation). (After Adamson et al. 2006)

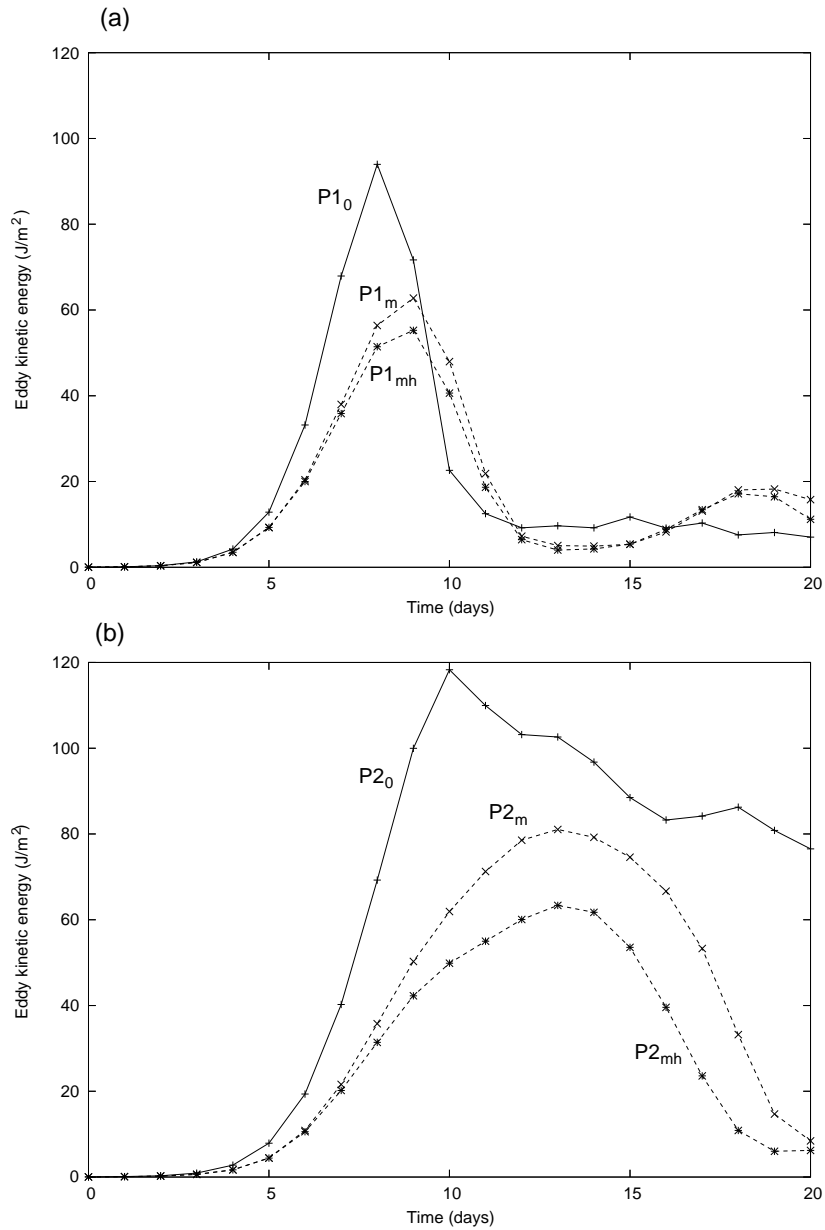


Figure 2: The domain-averaged eddy kinetic energy with and without parameterized turbulent fluxes of heat and momentum during (a) LC1 and (b) LC2 model life cycles. The labelling for each model run is described in full in Sec. 2. Subscript 0 denotes a run without the boundary layer parameterization, whereas m and h indicate the inclusion of turbulent momentum and heat fluxes respectively.

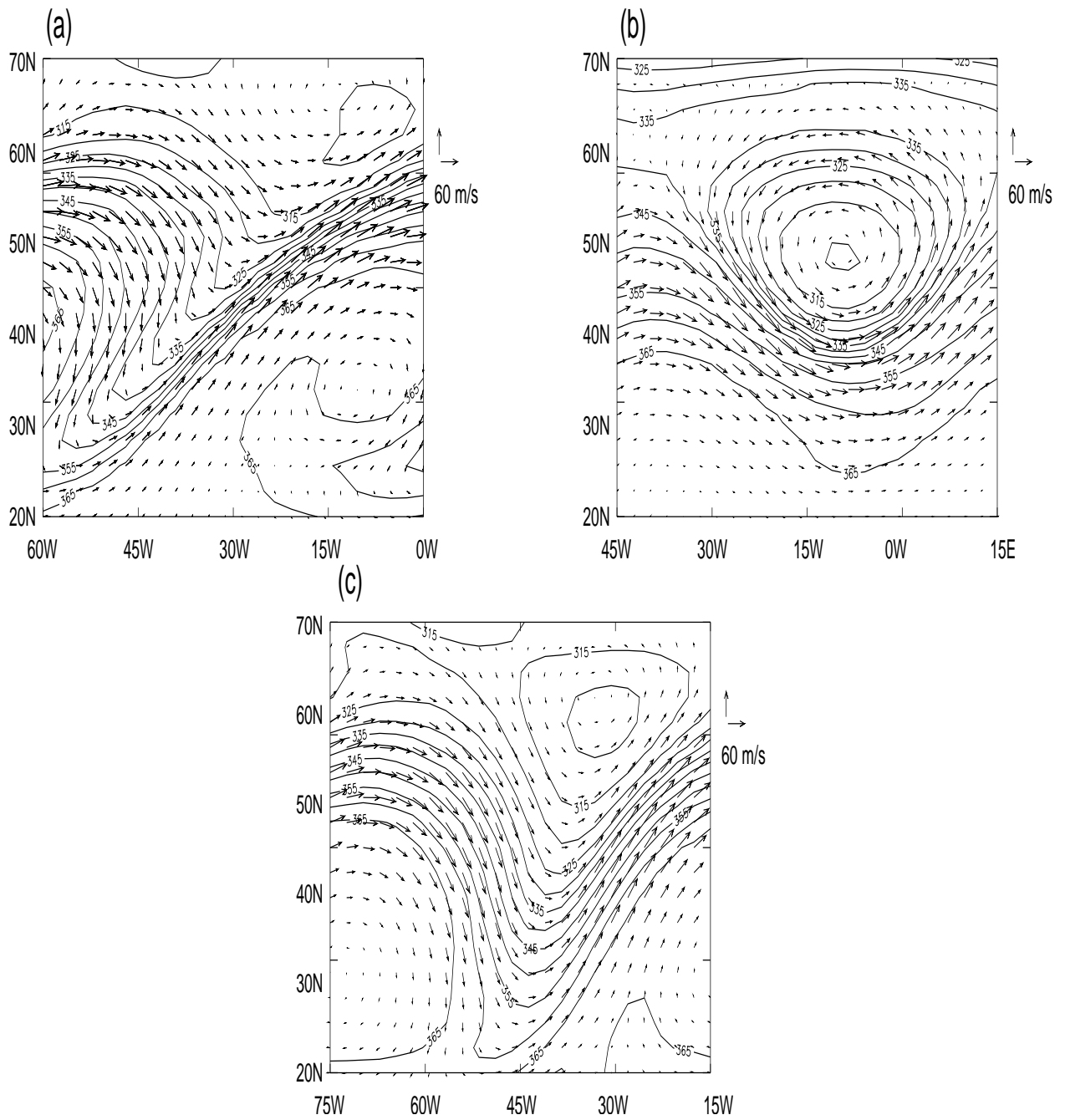


Figure 3: Potential temperature (5 K contour intervals) on the surface $PV = 2$ PVU in the early decay stage of runs (a) $P1_0$, (b) $P2_0$ and (c) $P2_m$. The elapsed time is nine days in (a), fifteen days in (b) and sixteen days in (c). Also shown are wind vectors on this surface, the scale for which appears in the top right.

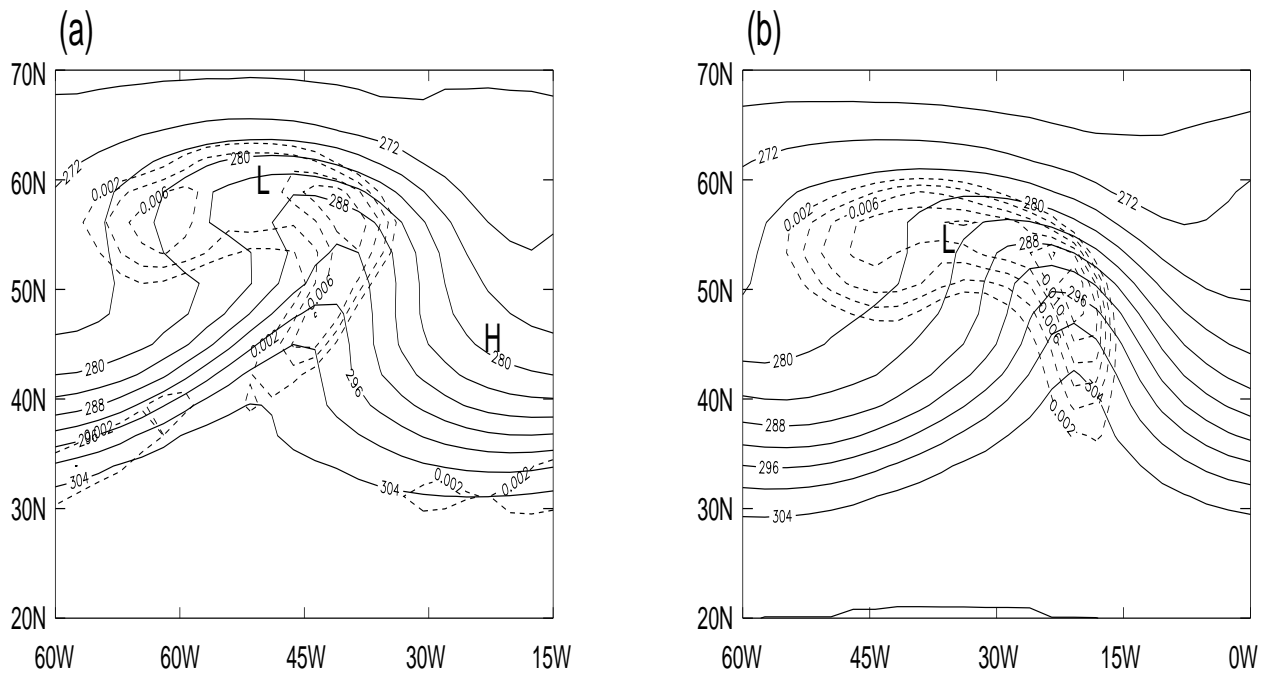


Figure 4: Potential temperature (4 K contour intervals) on the surface $\sigma = 0.92$ in the mid-growth stage of the runs (a) $P1_m$, and (b) $P2_m$. The elapsed time is six days in (a) and seven days in (b). Also shown is the Ekman pumping velocity (0.2 cm s^{-1} contour intervals for positive contours only; dashed). L and H denote the surface low and high pressure centers respectively. In (b) the highest pressure occurs to the north of the range of the figure.

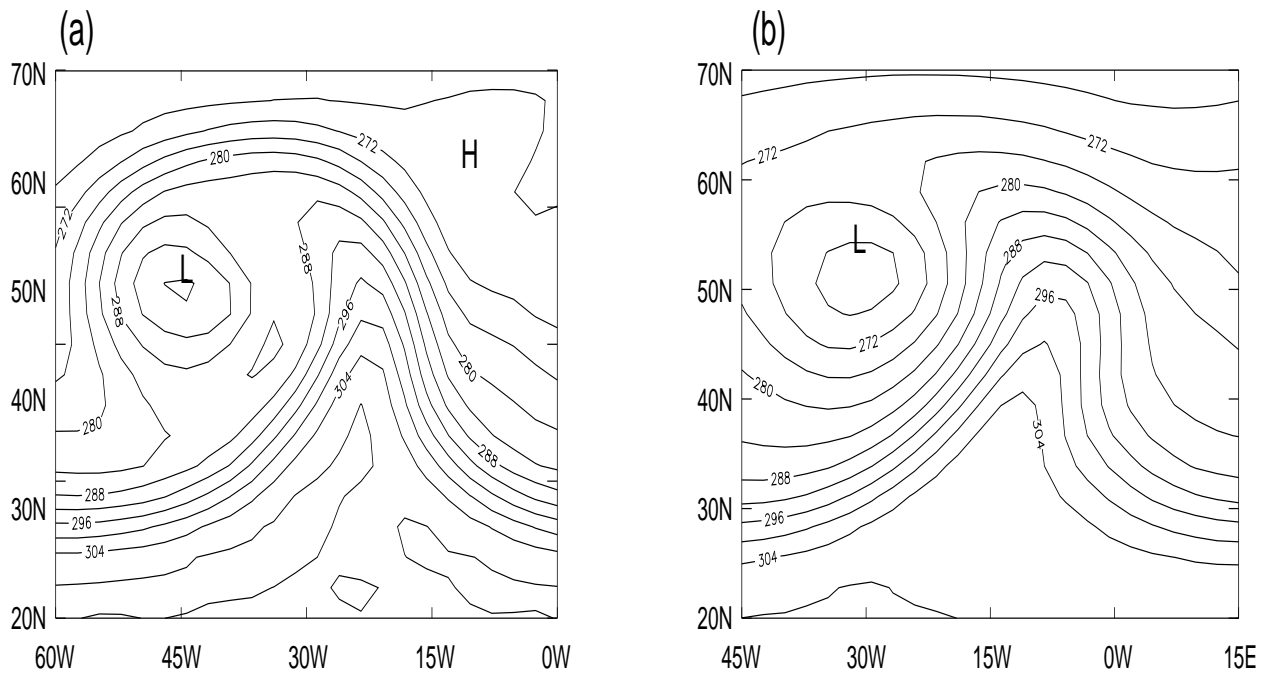


Figure 5: Potential temperature (4 K contour intervals) on the surface $\sigma = 0.92$ in the later growth stage of: (a) $P2_0$ and (b) $P2_m$. The elapsed time is eight days in (a) and nine days in (b). L and H denote the surface low and high pressure centers respectively. In (b) the highest pressure occurs to the north of the range of the figure.

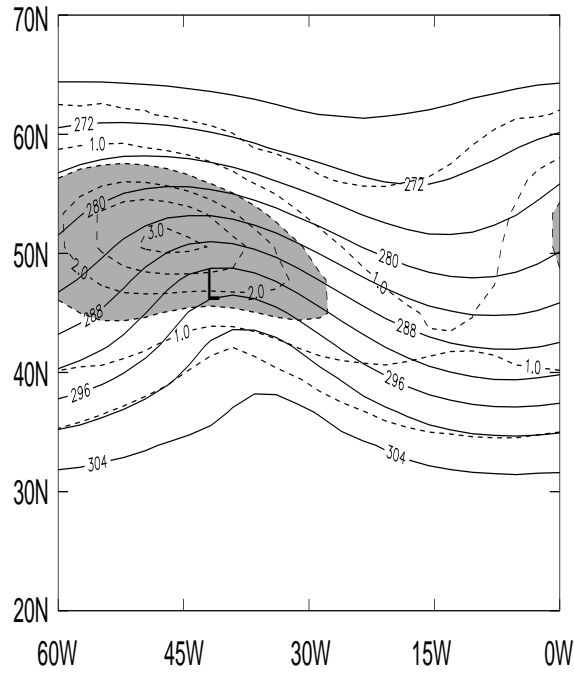


Figure 6: Potential temperature (4 K contour intervals) and PV (0.5 PVU contour intervals; dashed) in run $P2_m$ in the early growth stage on the surface $\sigma = 0.955$. The elapsed time is five days. PV values larger than 1.5 PVU are shaded. L denotes the surface low pressure center. The highest pressure occurs to the north of the range of the figure.

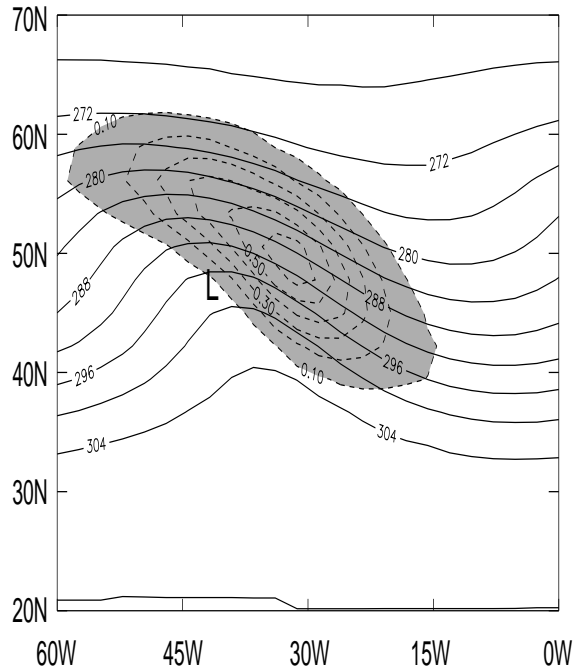


Figure 7: Boundary layer-averaged frictional generation of PV (0.1 PVU/d contour intervals; dashed) from the baroclinic generation term in the early growth stage of the run $P2_m$. The elapsed time is five days. The zero contour has been suppressed and generation rates larger in magnitude than 0.1 PVU/d are shaded, a darker shading being used for positive values. Also shown is the potential temperature (4 K contour intervals) on the surface $\sigma = 0.92$. L denotes the surface low pressure center. The highest pressure occurs to the north of the range of the figure.

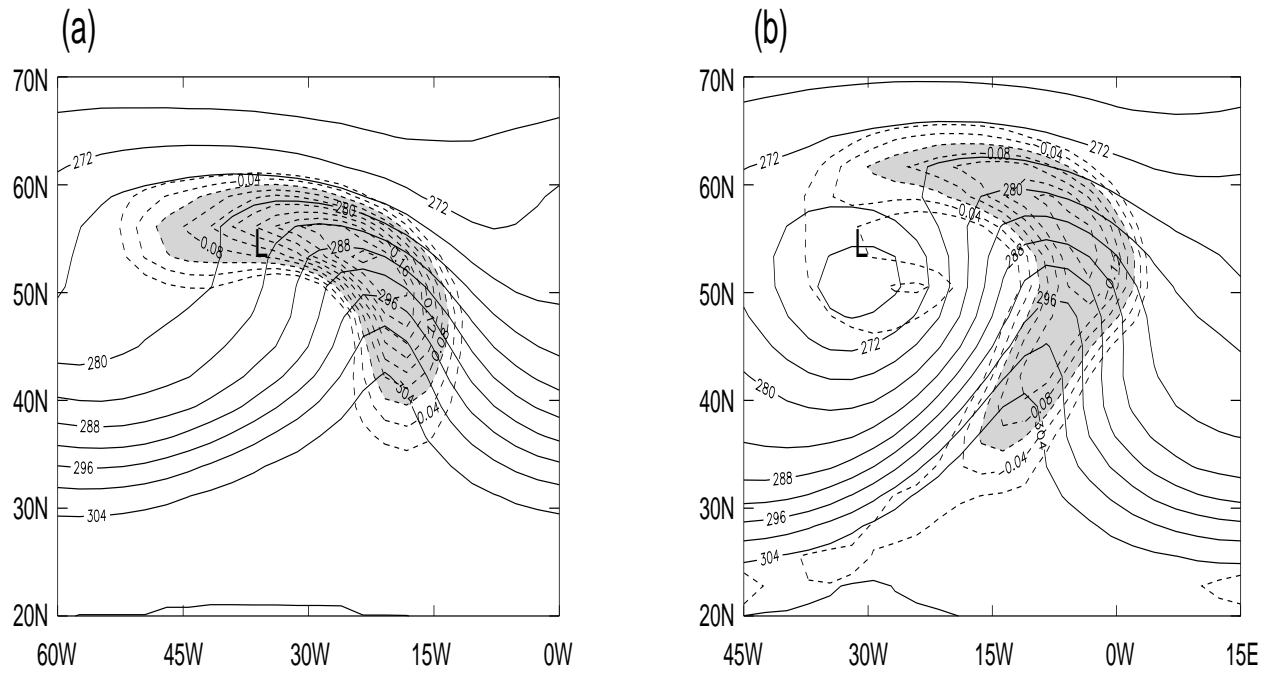


Figure 8: Ascent rate ω (0.02 Pas^{-1} contour intervals, negative values only; dashed) and potential temperature (4 K contour intervals) on the surface $\sigma = 0.92$ in run $P2_m$ in the (a) mid-growth and (b) later growth stages. The elapsed time is seven days in (a) and nine days in (b). L denotes the surface low pressure center. In both cases, the highest pressure occurs to the north of the range of the figure.

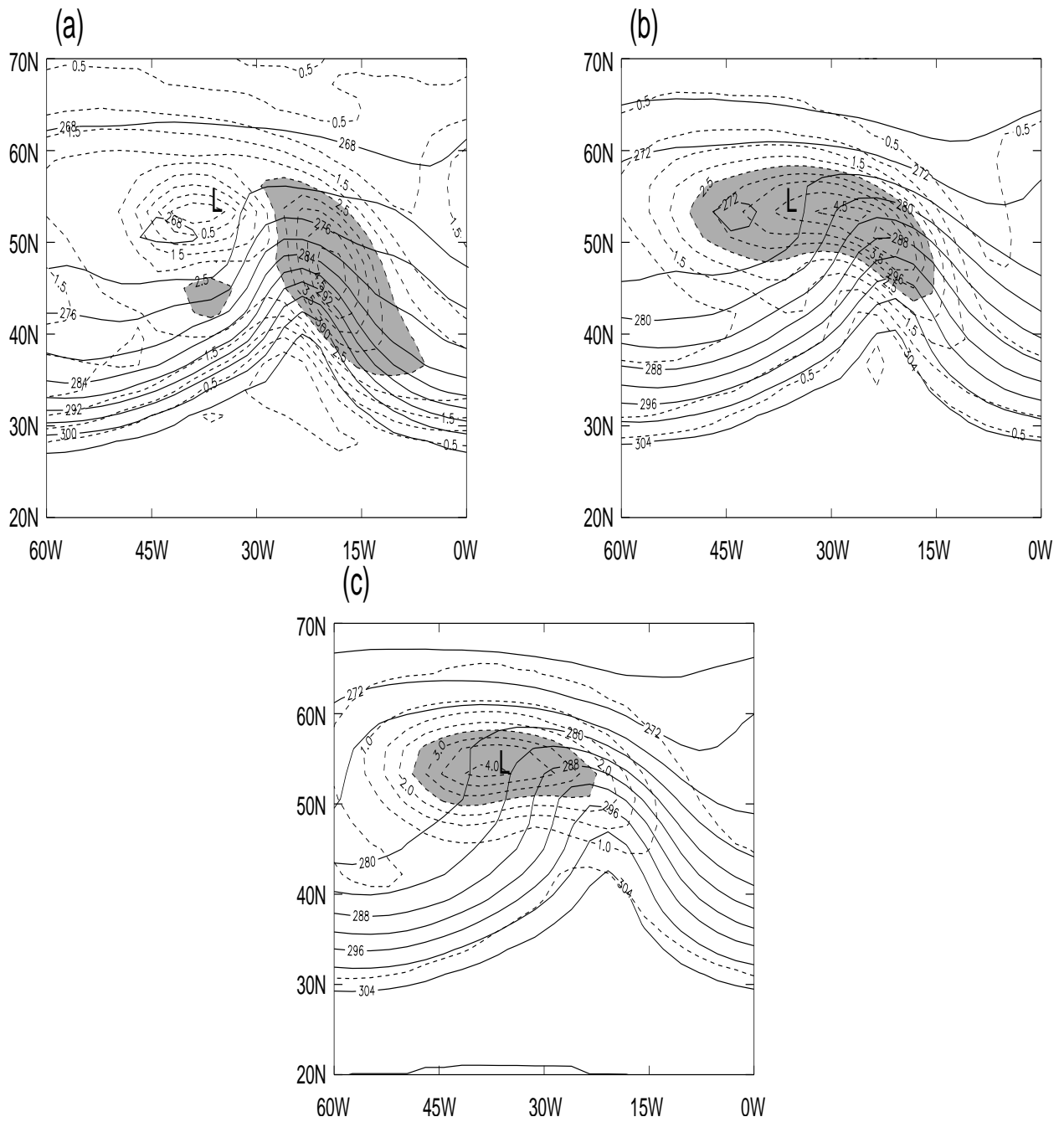


Figure 9: Potential temperature (4 K contour intervals) and PV (0.5 PVU contour intervals; dashed) in run $P2_m$ in the mid-growth stage on the surfaces (a) $\sigma = 0.98$, (b) $\sigma = 0.955$ and (c) $\sigma = 0.92$. The elapsed time is seven days. PV values larger than 2.5 PVU are shaded. L denotes the surface low pressure center. The highest pressure occurs to the north of the range of the figure.

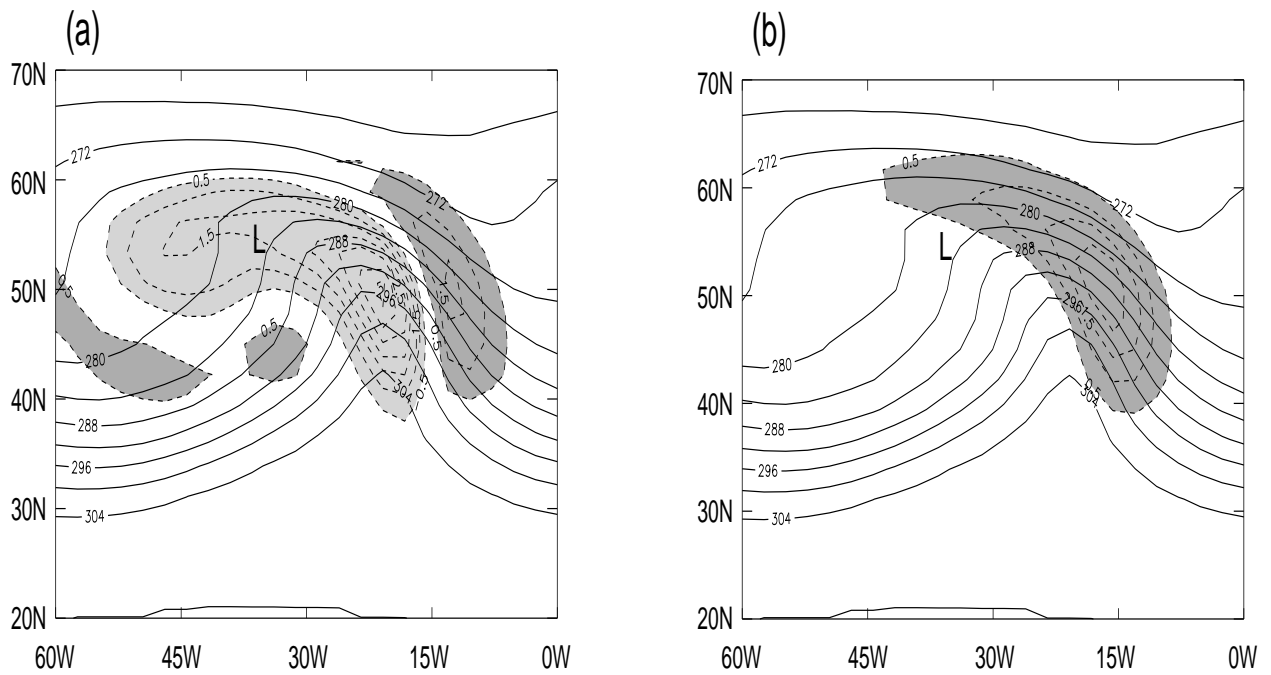


Figure 10: Boundary layer-averaged frictional generation of PV (0.5 PVU/d contour intervals; dashed) in the mid-growth stage of run $P2_m$: (a) barotropic generation term and (b) baroclinic generation term. The elapsed time is seven days. The zero contour has been suppressed and generation rates larger in magnitude than 0.5 PVU/d are shaded, a darker shading being used for positive values. Also shown is the potential temperature (4 K contour intervals) on the surface $\sigma = 0.92$. L denotes the surface low pressure center. The highest pressure occurs to the north of the range of the figure.

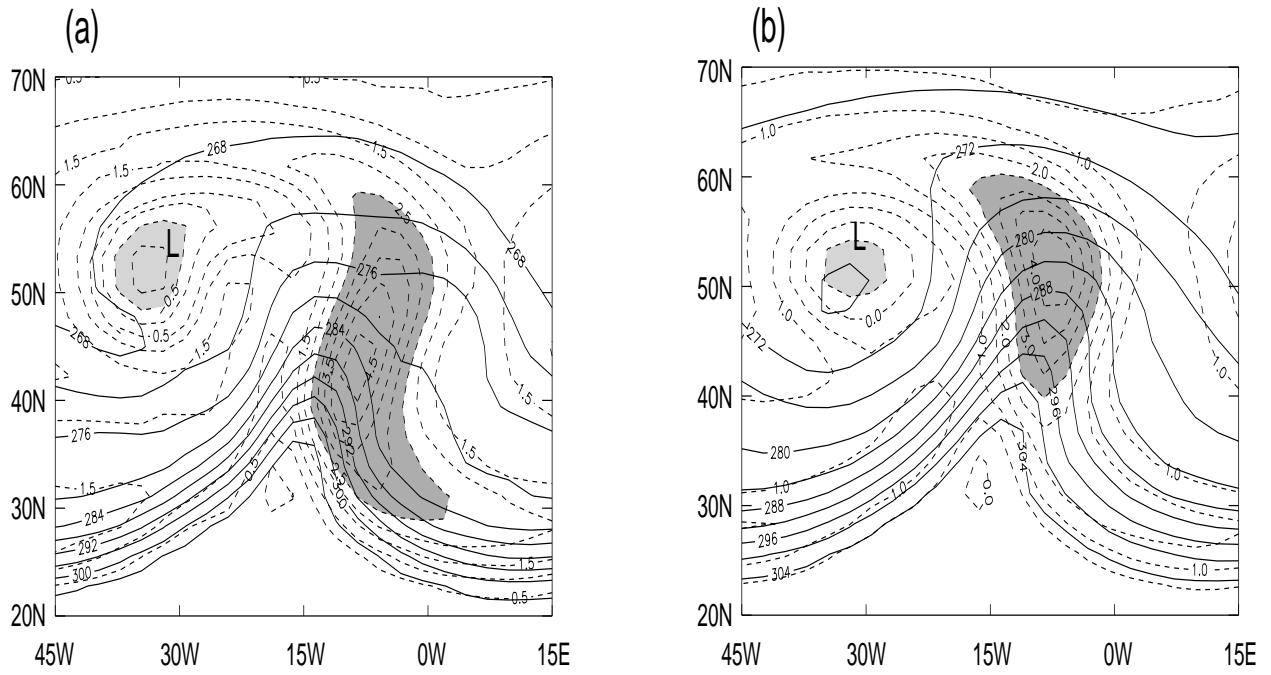


Figure 11: Potential temperature (4 K contour intervals) and PV (0.5 PVU contour intervals; dashed) in run $P2_m$ in the later growth stage on the surfaces (a) $\sigma = 0.98$ and (b) $\sigma = 0.955$. The time elapsed is nine days. PV values larger than 2.5 PVU and smaller than -0.5 PVU are shaded, a darker shading being used in the former case. L denotes the surface low pressure center. The highest pressure occurs to the north of the range of the figure.

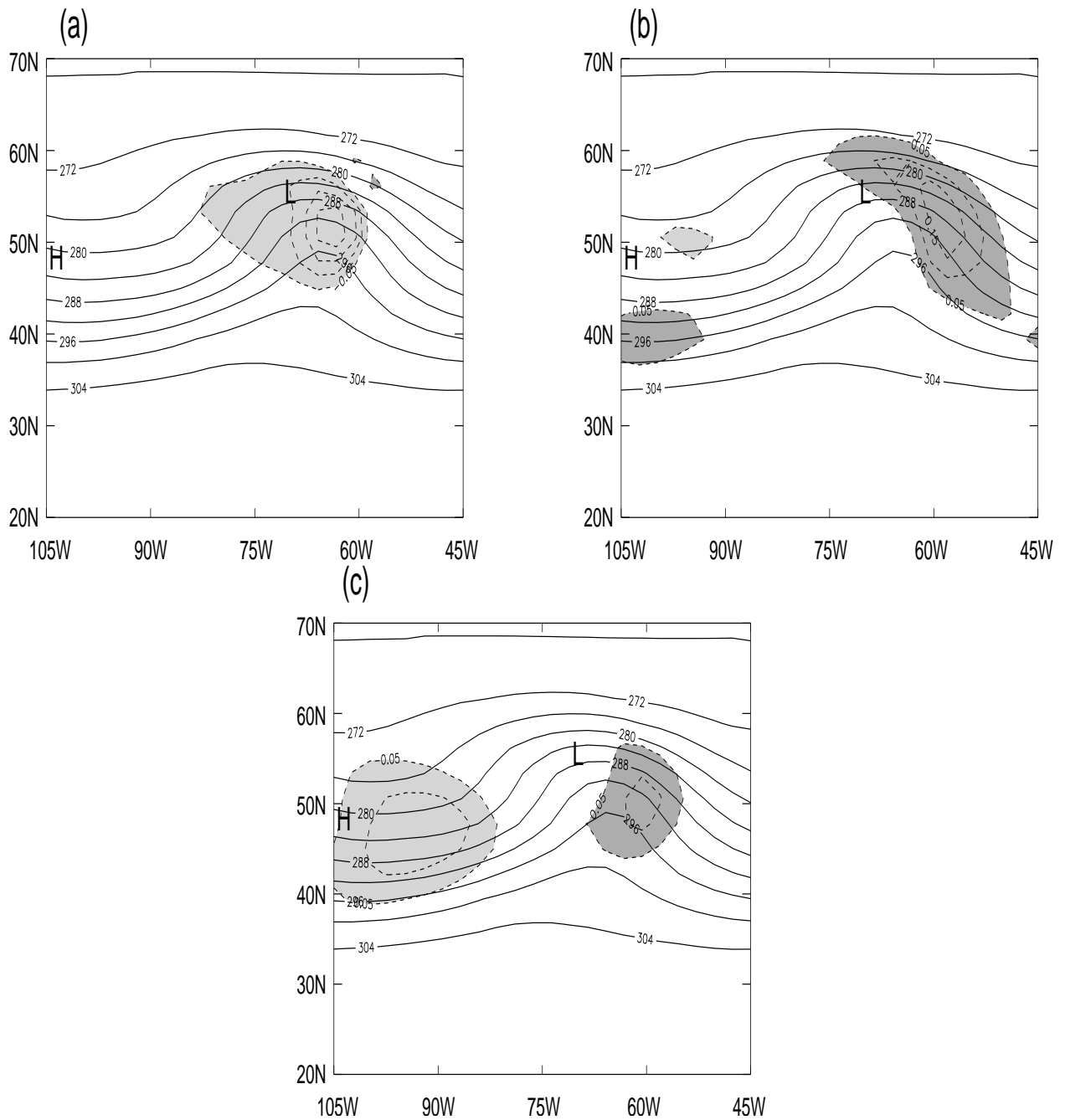


Figure 12: Boundary layer-averaged generation of PV (0.05 PVU/d contour intervals; dashed) in the early growth stage of run $P1_{mh}$: (a) barotropic frictional generation term, (b) baroclinic frictional generation term, (c) barotropic heat-flux generation term. The time elapsed is four days. The zero contour has been suppressed and generation rates larger in magnitude than 0.05 PVU/d are shaded, a darker shading being used for positive values. Also shown is the potential temperature (4 K contour intervals) on the surface $\sigma = 0.92$. L and H denote the surface low and high pressure centers.

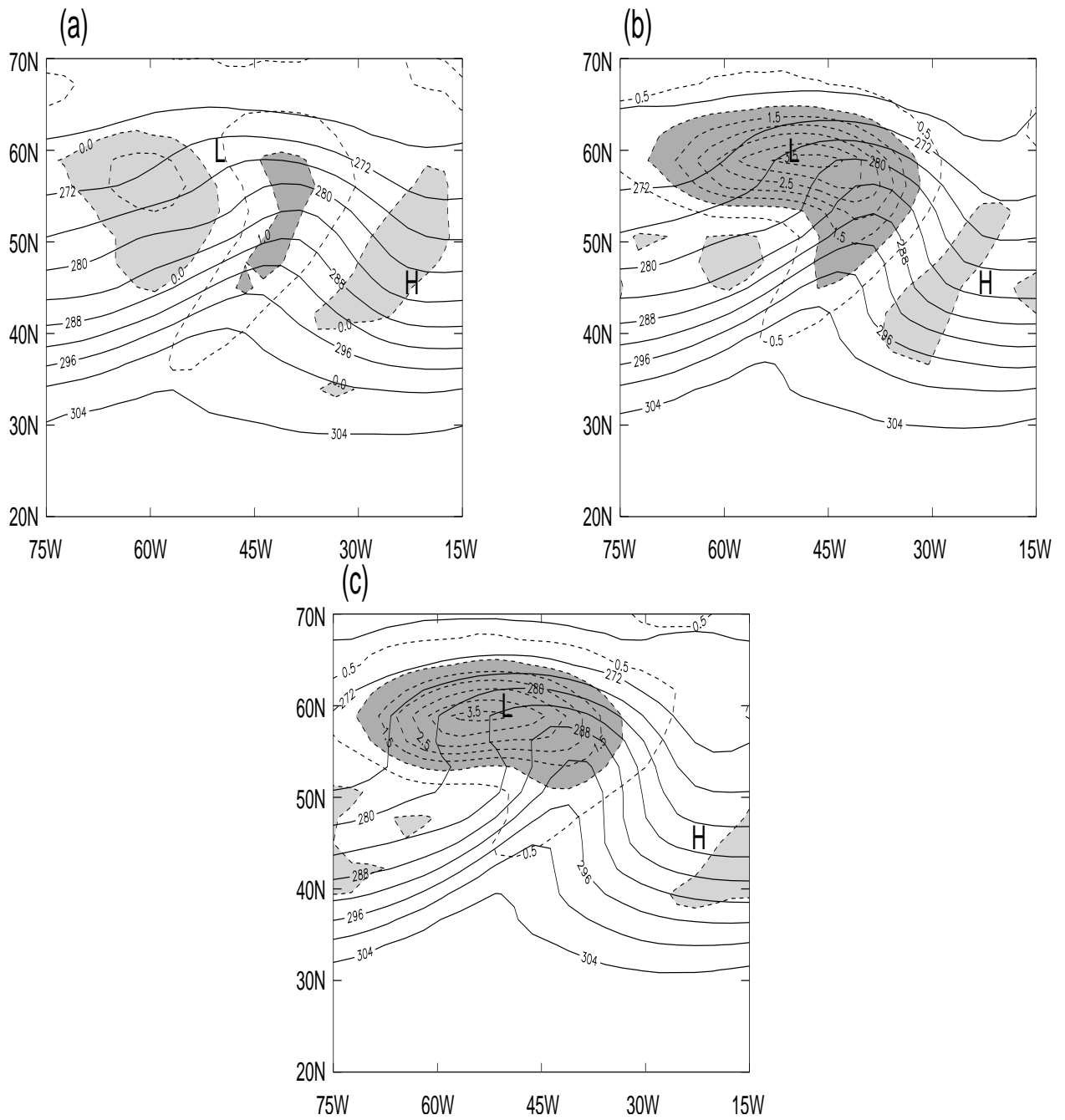


Figure 13: Potential temperature (4 K contour intervals) and PV (0.5 PVU contour intervals; dashed) in run $P1_{mh}$ in the mid-growth stage on the surfaces (a) $\sigma = 0.98$, (b) $\sigma = 0.955$ and (c) $\sigma = 0.92$. The time elapsed is six days. PV values larger than 1 PVU and smaller than 0 PVU are shaded, a darker shading being used in the former case. L and H denote the surface low and high pressure centers.

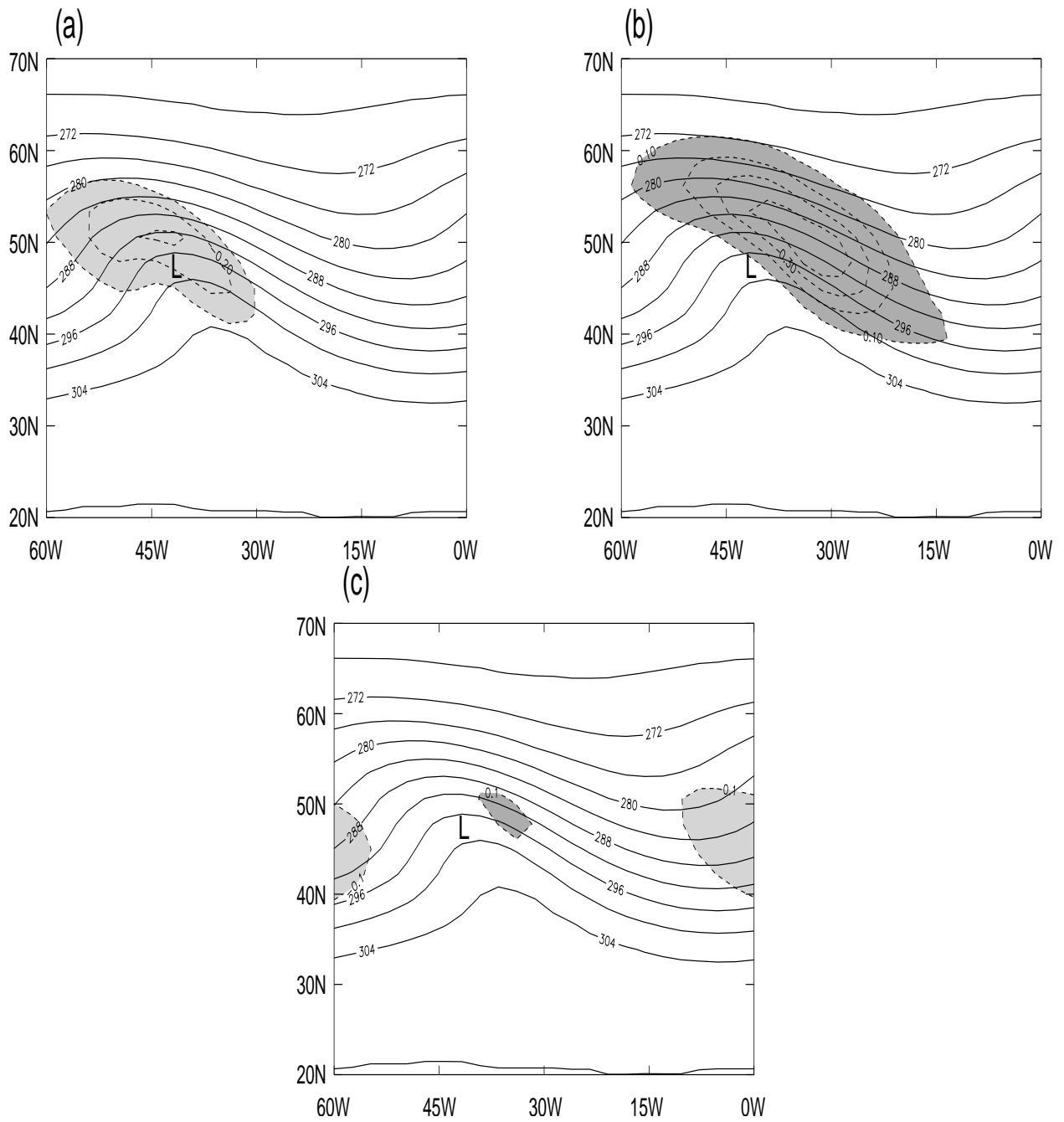


Figure 14: Boundary layer-averaged generation of PV (0.1 PVU/d contour intervals; dashed) in the early growth stage of run $P2_{mh}$: (a) barotropic frictional generation term, (b) baroclinic frictional generation term and (c) barotropic heat-flux generation term. The elapsed time is five days. The zero contour has been suppressed and generation rates larger in magnitude than 0.1 PVU/d are shaded, a darker shading being used for positive values. Also shown is the potential temperature (4 K contour intervals) on the surface $\sigma = 0.92$. L denotes the surface low pressure center. The highest pressure occurs to the north of the range of the figure.

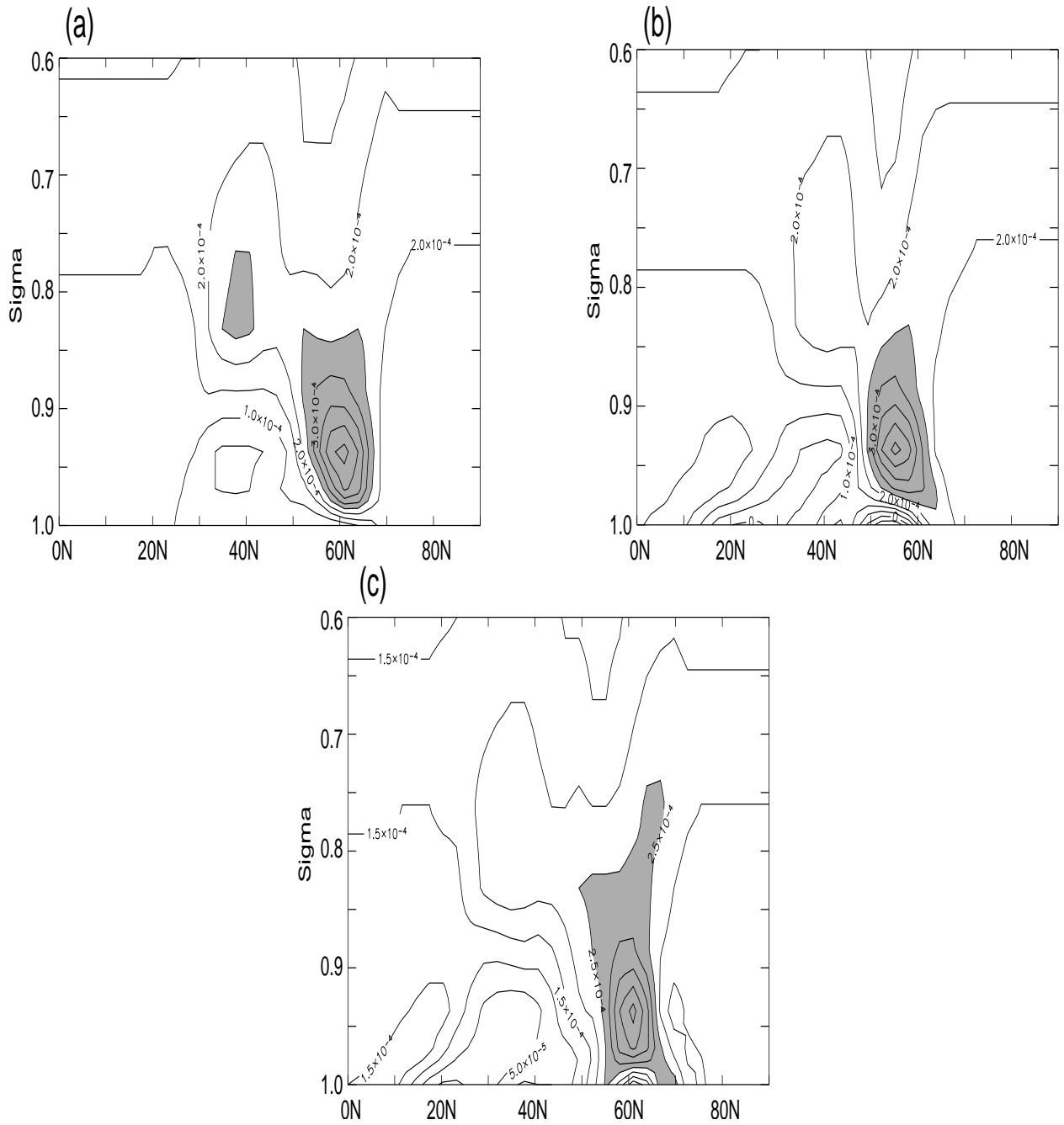


Figure 15: Zonal-mean static stability ($5 \times 10^{-5} \text{ s}^{-2}$ contour interval) in the (a) later growth stage of run $P1_{mh}$, (b) mid-growth stage of run $P2_{mh}$ and (c) later growth stage of run $P2_{mh}$. The elapsed time is seven days in (a), seven days in (b) and nine days in (c). Stabilities larger than $2.5 \times 10^{-4} \text{ s}^{-2}$ are shaded.

List of Tables

- 1 Energy losses after 20 days of integration, using the basic state as the initial state. The run label is constructed from the basic state used, and whether or not parameterized turbulent momentum and heat fluxes were included. See text for details. Energy lost is given as an absolute value, as a fraction of the total initial-state energy and as a fraction of the maximum eddy energy obtained from the corresponding run with the normal mode added to the initial state. 53
- 2 Equivalent times (at the end of the nearest whole day) in the life cycles of each model run. The times of early, mid- and later growth occur for an eddy kinetic energy that is, respectively, 5, 33 and 67% of its peak value. The early decay time occurs for an eddy kinetic energy that has fallen to 75% of its peak value. 54

Table 1: Energy losses after 20 days of integration, using the basic state as the initial state. The run label is constructed from the basic state used, and whether or not parameterized turbulent momentum and heat fluxes were included. See text for details. Energy lost is given as an absolute value, as a fraction of the total initial-state energy and as a fraction of the maximum eddy energy obtained from the corresponding run with the normal mode added to the initial state.

Run label	Initial state	Momentum fluxes	Heat fluxes	Energy lost (kJm ⁻²)	Fraction of total (%)	Fraction of eddy energy (%)
A1 ₀	LC1	No	No	12.8	0.07	1.17
A1 _m	LC1	Yes	No	61.0	0.32	8.16
A1 _{mh}	LC1	Yes	Yes	38.7	0.20	5.91
A2 ₀	LC2	No	No	10.5	0.06	0.78
A2 _m	LC2	Yes	No	184.5	0.98	18.72
A2 _{mh}	LC2	Yes	Yes	104.9	0.56	13.82

Table 2: Equivalent times (at the end of the nearest whole day) in the life cycles of each model run. The times of early, mid- and later growth occur for an eddy kinetic energy that is, respectively, 5, 33 and 67% of its peak value. The early decay time occurs for an eddy kinetic energy that has fallen to 75% of its peak value.

Run label	Early growth	Mid-growth	Later growth	Peak	Early decay
P1 ₀	4	6	7	8	9
P1 _m	4	6	7	9	10
P1 _{mh}	4	6	7	9	10
P2 ₀	5	7	8	10	15
P2 _m	5	7	9	13	16
P2 _{mh}	5	7	9	13	15